

# Discovery of a $z \simeq 4.9$ Lyman- $\alpha$ Emitter Protocluster: Wavelength-Dependent Environmental Effects on Galaxy Structure

RONALDO LAISHRAM <sup>1</sup>, YUSEI KOYAMA <sup>1,2</sup>, HARUKA KUSAKABE <sup>3</sup>, SATOSHI KIKUTA <sup>4</sup>, SHUNTA SHIMIZU <sup>4</sup> AND TADAYUKI KODAMA <sup>5</sup>

<sup>1</sup>*National Astronomical Observatory of Japan, 2-21-1 Osawa, Mitaka, Tokyo 181-8588, Japan*

<sup>2</sup>*Department of Astronomical Science, The Graduate University for Advanced Studies, 2-21-1 Osawa, Mitaka, Tokyo 181-8588, Japan*

<sup>3</sup>*Department of General Systems Studies, Graduate School of Arts and Sciences, The University of Tokyo, 3-8-1 Komaba, Meguro-ku, Tokyo, 153-8902, Japan*

<sup>4</sup>*Department of Astronomy, School of Science, The University of Tokyo, 7-3-1, Hongo, Bunkyo, Tokyo 113-0033, Japan*

<sup>5</sup>*Astronomical Institute, Tohoku University, 6-3, Aramaki, Aoba, Sendai, Miyagi 980-8578, Japan*

Submitted to ApJL

## ABSTRACT

We report the discovery of a Lyman- $\alpha$  emitter (LAE) protocluster at  $z = 4.90$  in the COSMOS field, comprising four distinct overdensity peaks spanning  $\sim 65 \times 36$  cMpc<sup>2</sup>, with the primary concentration exhibiting a 4-fold surface density enhancement relative to the field within a 1.5 proper Mpc (pMpc) radius. Using SILVERRUSH narrowband survey data combined with JWST COSMOS-Web imaging, we perform a first systematic rest-frame optical and UV morphological comparison of protocluster versus field LAEs at this redshift using JWST NIRCcam rest-frame UV (F150W,  $\sim 2540\text{\AA}$ ) and optical (F277W,  $\sim 4700\text{\AA}$ ) imaging. Sérsic profile fitting for 16 protocluster members and 23 field LAEs reveals a significant size difference: protocluster LAEs are  $\sim 40\%$  larger in rest-optical (median  $R_e = 0.81^{+0.26}_{-0.04}$  kpc vs.  $0.58^{+0.11}_{-0.04}$  kpc,  $p = 0.041$ ) with no significant difference in rest-UV ( $p = 0.51$ ) or Sérsic index. At fixed stellar mass, protocluster LAEs are offset by  $+0.12$  dex ( $\simeq 31\%$ ) in rest-optical size from the field size-mass relation (68% CI:  $[+0.08, +0.21]$ ; Mann-Whitney  $p = 0.033$ ), with 75% exhibiting positive size residuals compared to 44% of field LAEs. This wavelength-dependent environmental signature suggests that protocluster environments at  $z \simeq 5$  preferentially affect extended stellar populations, possibly through tidal interactions or an earlier onset of star formation in the dense environment, with no significant environmental difference detected in rest-UV sizes, providing observational evidence for environmental influences on the structure of LAEs during the early build-up phase of cosmic star formation.

*Keywords:* Lyman-alpha galaxies (978); Protoclusters (1297); Galaxy environments (2029); Galaxy structure (622); High-redshift galaxy clusters (2007)

## 1. INTRODUCTION

Galaxy protoclusters represent the progenitors of the most massive structures in the present-day Universe, providing critical laboratories for investigating the onset of environmental influences on galaxy evolution. While the morphology-density relation is well-established in

local clusters (Dressler 1980), determining when environmental processes begin to shape galaxy structure remains a fundamental question in observational cosmology. At  $z \simeq 5$ , during the early build-up phase of cosmic star formation, protoclusters occupy a unique position where hierarchical assembly is ongoing and are predicted to evolve into massive clusters by  $z = 0$  (Chiang et al. 2017; Ata et al. 2022). In these dense regions, mechanisms such as enhanced mergers, tidal interactions, and gas accretion are predicted to leave their first observable signatures on member galaxies (Boselli & Gavazzi

2006; Overzier 2016). Identifying and characterizing these structures at such early epochs is therefore essential for constraining when dense environments begin to regulate galaxy properties.

Lyman- $\alpha$  emitters (LAEs) serve as highly efficient tracers of protoclusters due to their ubiquity and established clustering properties at early cosmic times (Ouchi et al. 2018; Kusakabe et al. 2018; Higuchi et al. 2019; Ouchi et al. 2020; Hu et al. 2021; Ramakrishnan et al. 2024). Narrowband imaging surveys have successfully mapped LAE overdensities across a wide range of epochs (Lee et al. 2014a; Bădescu et al. 2017; Lee et al. 2024). Shimasaku et al. (2003) discovered the first proto-large-scale structure traced by LAEs at  $z \approx 4.86$  in the Subaru Deep Field, revealing an elongated overdense region spanning  $\sim 65$  comoving Mpc. Subsequent surveys have extended these discoveries to lower redshifts, including Bădescu et al. (2017)’s identification of the Boötes protocluster at  $z = 2.3$  and Huang et al. (2022)’s mapping of the Hyperion complex at  $z = 2.47$ , as well as within the COSMOS field itself at intermediate epochs, exemplified by Capak et al. (2011)’s discovery at  $z = 5.3$  surrounding the submillimeter source AzTEC3, and recent identifications of complex structures at  $z \simeq 4.5$  (Staab et al. 2024; Rubet et al. 2025). At the highest redshifts approaching the epoch of reionization, Hu et al. (2021) identified LAGER-z7OD1 at  $z \approx 6.9$ , while Ramakrishnan et al. (2023) demonstrated that LAEs and Lyman- $\alpha$  blobs preferentially reside in overdense regions associated with protoclusters. These structures exhibit characteristic surface density enhancements that are approximately 3–6 times higher than those in field regions.

While the spatial clustering of LAEs has been extensively characterized, their morphological properties, particularly in dense protocluster environments, remain poorly constrained at  $z \gtrsim 4$ . Previous *HST* studies have revealed that LAEs are compact systems with effective radii ranging from  $\sim 100$ – $200$  pc at  $z \simeq 2$ – $3$  (Kim et al. 2026) to  $R_e \lesssim 1$  kpc at higher redshifts (Bond et al. 2012; Shibuya et al. 2019). While studies of the Ly $\alpha$  luminosity function and equivalent width distribution in protoclusters at  $z \simeq 3.8$  find these properties to be largely independent of environment (Malavasi et al. 2021), structural properties may be more sensitive to the frequent mergers and interactions characterizing these dense regions. However, systematic comparisons of LAE morphologies between protocluster and field environments at these early epochs have not been conducted. Furthermore, *HST* observations at  $z \gtrsim 5$  are restricted to rest-frame UV wavelengths, which trace recent star formation but may not reflect the underlying stellar mass distribution shaped by environmental

processes. Although numerous studies have identified LAE overdensities at  $z \simeq 4$ – $6$ , quantitative comparisons of rest-frame optical structural parameters (e.g., effective radii, Sérsic indices) between protocluster and field LAEs remain absent at these redshifts.

The advent of JWST has transformed this landscape by enabling high-resolution imaging at rest-frame optical wavelengths for  $z > 4$  galaxies (Casey et al. 2023). Recent studies suggest that overdensities may accelerate the emergence of evolved galaxy properties even at these early epochs (Morishita et al. 2025). This capability enables direct measurements of stellar mass distributions in high-redshift protoclusters, decoupling young UV-bright star-forming regions from extended older stellar populations. Determining whether galaxy sizes and structural parameters depend on local density at these early epochs is critical for establishing when and how environmental mechanisms begin to regulate stellar mass assembly.

In this Letter, we report the discovery of an LAE protocluster at  $z = 4.90$  in the COSMOS field, identified from the Systematic Identification of LAEs for Visible Exploration and Reionization Research Using Subaru HSC (SILVERRUSH) narrowband survey (Kikuta et al. 2023). The structure comprises four distinct overdensity peaks spanning  $\sim 65 \times 36$  cMpc<sup>2</sup>, with surface density enhancements of up to a factor of 4 relative to the field within 1.5 pMpc radii of each peak. We refer to this system as the Loktak protocluster, after Loktak Lake in Manipur, India, whose floating islands within an interconnected body of water evoke the multi-component nature of this large-scale structure. Leveraging deep NIRCcam imaging from the JWST COSMOS-Web treasury survey (Casey et al. 2023; Franco et al. 2024), we perform one of the first systematic rest-frame optical structural comparisons of protocluster versus field LAEs at  $z \simeq 5$ . We measure effective radii in rest-frame UV (F150W) and rest-frame optical (F277W) through Sérsic profile fitting to investigate wavelength-dependent structural properties and constrain how the densest environments at cosmic dawn influence galaxy structure. Throughout this work, we adopt a flat  $\Lambda$ CDM cosmology with  $\Omega_m = 0.3$ ,  $\Omega_\Lambda = 0.7$ , and  $H_0 = 70$  km s<sup>-1</sup> Mpc<sup>-1</sup>, and quote magnitudes in the AB system.

## 2. DATA

### 2.1. Ly $\alpha$ Emitter Sample

Our parent sample of LAEs at  $z \simeq 4.9$  is drawn from the SILVERRUSH program (Ouchi et al. 2018; Shibuya et al. 2018; Kikuta et al. 2023), which identified LAEs using narrowband (NB) imaging from the Hyper Suprime-Cam Subaru Strategic Program (HSC-SSP;

Aihara et al. 2022) and the Cosmic Hydrogen Reionization Unveiled with Subaru (CHORUS) survey (Inoue et al. 2020). The HSC-SSP is a multi-tier wide-field imaging survey, with its Deep layer covering an effective area of  $\sim 25 \text{ deg}^2$  (after masking low S/N regions and bad pixels) with broadband (grizy) and NB filters, utilizing the  $1.77 \text{ deg}^2$  field-of-view of HSC on the 8.2 m Subaru Telescope (Aihara et al. 2019, 2022). CHORUS complements HSC-SSP with deeper NB imaging in the COSMOS field using custom filters including NB718. The combined SILVERRUSH XIII catalog (Kikuta et al. 2023) contains 726 photometrically selected LAEs in the NB718 filter ( $\lambda_c = 7170 \text{ \AA}$ , FWHM =  $111 \text{ \AA}$ ) covering  $1.76 \text{ deg}^2$  in the COSMOS field, targeting Ly $\alpha$  emission at  $z = 4.90 \pm 0.046$ .

LAE candidates were selected via narrowband excess (NB – BB color) with  $> 5\sigma$  detection significance in NB718, combined with Lyman break color criteria using multi-band photometry to reject low-redshift interlopers (Ouchi et al. 2018; Kikuta et al. 2023). Source detection and photometry were performed on PSF-matched coadded images processed with hscPipe version 8, with limiting magnitudes measured on a patch-by-patch basis to ensure uniform selection across the survey area. Full details of the data reduction, photometric selection criteria, masking procedures, and visual inspection are provided in Kikuta et al. (2023). The SILVERRUSH catalog includes 13 spectroscopically confirmed LAEs at  $z \simeq 4.9$  in the COSMOS field, validating the photometric selection.

### 2.2. JWST COSMOS-Web Imaging Data

We utilized deep near-infrared imaging from the COSMOS-Web program (Casey et al. 2023), a JWST Cycle 1 treasury survey that mapped  $0.54 \text{ deg}^2$  of the COSMOS field with NIRCcam and  $0.19 \text{ deg}^2$  with MIRI. The NIRCcam observations employ four broadband filters—F115W, F150W, F277W, and F444W—reaching  $5\sigma$  point-source sensitivities of 26.6–27.3 mag, 26.9–27.7 mag, 27.5–28.2 mag, and 27.5–28.2 mag, respectively, measured in  $0''.15$  diameter apertures. MIRI observations in F770W achieve depths of 25.33–25.98 mag within  $0''.3$  apertures.

Observations were executed across multiple epochs between 2023 January and 2024 May, with the majority completed during three primary windows: 2023 January, 2023 April, and 2023 December/2024 January. Full details of the image processing and mosaic construction are provided by Franco et al. (2024, 2025) for NIRCcam and Harish et al. (2025) for MIRI. The final NIRCcam mosaics are available at pixel scales of both 30 mas and 60 mas; we adopt the higher-resolution 30 mas mosaics for our

structural measurements to optimize spatial sampling of compact high-redshift sources.

At  $z = 4.90$ , the four NIRCcam filters probe rest-frame wavelengths of approximately 1950  $\text{\AA}$  (F115W), 2540  $\text{\AA}$  (F150W), 4700  $\text{\AA}$  (F277W), and 7500  $\text{\AA}$  (F444W). The F150W filter traces rest-frame UV continuum emission dominated by young stellar populations, while F277W and F444W sample rest-frame optical light sensitive to stellar mass and older populations.

### 2.3. Photometric Catalog and Derived Physical Properties

We obtained stellar masses and star formation rates (SFRs) from the COSMOS-Web photometric catalog presented by Shuntov et al. (2025), which provides multi-wavelength photometry and spectral energy distribution (SED) fitting results for all detected sources in the survey footprint. The catalog employs the LEPHARE SED-fitting code (Arnouts et al. 2002; Ilbert et al. 2006) to derive photometric redshifts and physical parameters from composite photometry spanning 32 bands from  $\sim 0.3 \mu\text{m}$  to  $\sim 8 \mu\text{m}$  (Shuntov et al. 2025).

Template fitting is based on Bruzual & Charlot (2003) stellar population synthesis models incorporating varied star formation histories, stellar ages, metallicities, and dust attenuation prescriptions (Calzetti et al. 2000). For each source, LEPHARE computes a probability density function of the photometric redshift; physical properties (stellar mass, SFR) are then calculated at the median photometric redshift. Shuntov et al. (2025) demonstrate that LEPHARE-derived stellar masses show good agreement with independent CIGALE estimates (Bouquien et al. 2019), providing confidence in the adopted values. We adopt stellar masses from the LEPHARE fits for consistency with the published COSMOS-Web catalog.

### 2.4. Spectroscopic Redshift Compilation

To validate photometric redshifts and identify potential contamination in our LAE sample, we cross-referenced our sources with the COSMOS spectroscopic redshift compilation of Khostovan et al. (2026). This compilation aggregates 487,666 spectroscopic redshift measurements for 266,284 unique galaxies from 138 spectroscopic programs observed over two decades within a  $10 \text{ deg}^2$  area centered on the COSMOS field, spanning redshifts from the local Universe to  $z \simeq 8$ . The catalog provides robust spectroscopic coverage for low- and intermediate-mass star-forming galaxies and massive quiescent systems at  $z < 1.25$ , as well as low-mass star-forming galaxies at  $z > 2$ .

We cross-matched our NB718 LAE catalog with the COSMOS-Web NIRCcam imaging using a matching ra-

dius of  $0''.5$  following Shuntov et al. (2025), yielding 215 initial LAE candidates with JWST detections. To ensure sample purity, we implemented a two-stage cleaning procedure. First, we cross-referenced all candidates with the COSMOS spectroscopic redshift compilation (Khostovan et al. 2026) to identify and remove contaminants confirmed at discrepant redshifts. Within the  $0.54 \text{ deg}^2$  COSMOS-Web survey footprint, this compilation contains 49 spectroscopically confirmed galaxies at  $z = 4.90 \pm 0.046$  (the NB718 transmission window) with quality flags  $\geq 3$  (reliable or very secure redshifts); of these, eight are positionally matched to our LAE candidates, providing direct validation of the narrowband selection. Second, we applied photometric redshift quality cuts using the COSMOS-Web LEPHARE-derived redshifts (Shuntov et al. 2025), retaining only sources with photometric redshifts consistent with the NB718 selection window within  $\Delta z \leq 0.2$ . This threshold balances sample completeness against contamination from photometric redshift outliers, and we confirmed that our results are insensitive to moderate variations in this criterion. After applying these cuts, our final clean sample comprises 177 LAEs with robust redshift confirmation, which we adopt for all subsequent overdensity and morphological analyses. All eight spectroscopically confirmed LAEs pass our photometric redshift quality cuts and are retained in the final clean sample.

### 3. LARGE-SCALE OVERDENSITY STRUCTURE AT $Z = 4.90$

To characterize the environment of LAEs with JWST coverage within the  $0.54 \text{ deg}^2$  COSMOS-Web survey area, we measured local galaxy overdensity using two independent methods following established protocols (Ramella et al. 2001; Cooper et al. 2005; Darvish et al. 2015): (1) the fifth nearest neighbor distance, which measures the projected distance to the fifth nearest LAE and calculates local surface density as  $\sigma_5 = 5/(\pi d_5^2)$  [ $\text{Mpc}^{-2}$ ], normalized to the dimensionless overdensity  $\delta_{\text{NN}} = \sigma_5/\langle\sigma_5\rangle - 1$ ; and (2) Voronoi tessellation, where each LAE defines a cell representing the region closer to it than to any other galaxy, with local density  $\rho_V = 1/A_{\text{cell}}$  [ $\text{Mpc}^{-2}$ ] normalized as  $\delta_V = \rho_V/\langle\rho_V\rangle - 1$ . Edge effects in the overdensity measurements are mitigated because the COSMOS-Web footprint is embedded within the larger SILVERRUSH/HSC survey area, ensuring all LAEs have complete neighbor coverage for environment calculations. Both methods yield consistent overdensity measurements across the field.

The resulting spatial distribution reveals a prominent large-scale overdensity structure at  $z \simeq 4.9$  (the Loktak protocluster). Figure 1 presents the overdensity map

constructed from these 177 LAEs. The structure exhibits a clear concentration of LAEs with multiple interconnected components, characteristic of protocluster environments in the early Universe.

To visualize the full spatial structure and identify overdensity peaks, we constructed a smoothed density field using Gaussian Kernel Density Estimation (KDE) following methods for mapping high-redshift structures (Lee et al. 2014b; Bădescu et al. 2017; Huang et al. 2022). We applied KDE with a bandwidth scaling factor of 0.3 to balance structure detail against noise, evaluated on a  $300 \times 300$  grid, and smoothed with a 2D Gaussian filter ( $\sigma = 1.5$  pixels). The primary peak, corresponding to the highest density concentration, is located at  $\text{RA} = 149.8412^\circ$ ,  $\text{Dec} = 2.2755^\circ$ . Figure 1 displays the resulting density map with contours marking relative density levels, with individual LAE positions overlaid.

The smoothed density map reveals four distinct peaks spanning  $\sim 65 \times 36 \text{ cMpc}^2$  on the sky. The primary peak exhibits the highest concentration. Three additional significant peaks are located at 7.6 pMpc to the east, 6.0 pMpc to the southeast, and 11.1 pMpc to the east, forming an extended structure suggestive of filamentary connections between density concentrations. Within 1.5 pMpc of the primary peak, 18 LAEs are enclosed, yielding a surface density of  $(36.9 \pm 8.7) \times 10^{-2} \text{ arcmin}^{-2}$ , signifying a 4-fold increase compared to the overall surveyed region ( $(9.11 \pm 0.62) \times 10^{-2} \text{ arcmin}^{-2}$  for 177 LAEs over  $0.54 \text{ deg}^2$ ); this enhancement rises to 5.5 times within 1.0 pMpc, indicating a steeply rising density profile toward the center. The three additional peaks show similar enhancements of 3, 2.8, and 2.5 times within their respective 1.5 pMpc radii, confirming the multi-component nature of the protocluster complex in an active phase of hierarchical assembly. Isodensity contour analysis independently confirms all four peaks with high statistical significance ( $4\text{--}12\sigma$ ), demonstrating the robustness of the structure identification.

Based on the overdensity measurements, we classify galaxies into distinct environmental samples for subsequent analysis. We define protocluster members as LAEs within a projected radius of 3.0 pMpc from the primary peak of the smoothed density field, yielding 28 candidate member LAEs. We confirmed that our results are consistent when adopting smaller membership radii (1.5 and 2.0 pMpc), though the larger radius provides a more statistically robust sample. Field LAEs are selected from the lowest density regions, defined as the bottom 25th percentile of the nearest neighbor overdensity distribution ( $\delta_{\text{NN}}$ ), yielding 44 galaxies. We focus on the primary peak as it exhibits the strongest overdensity ( $\sim 4$  times within 1.5 pMpc; Section 3); hereafter,

we refer to these 28 LAEs as protocluster members and the 44 low-density LAEs as field LAEs for all subsequent analysis.

To investigate environmental effects on galaxy structure, we measured morphologies of LAEs in the protocluster and field environments using GALFIT (Peng et al. 2002). We fit single Sérsic profiles to JWST NIR-Cam imaging in two filters: F150W, sampling rest-frame UV ( $\sim 2540\text{\AA}$ ), and F277W, sampling rest-frame optical ( $\sim 4700\text{\AA}$ ) at  $z = 4.90$ . Free parameters included the effective radius ( $R_e$ , containing half the total light), Sérsic index ( $n$ , describing profile concentration), total magnitude, and centroid position. Each fit was convolved with an empirical PSF constructed from stacking unsaturated stars in the field. We retain only galaxies whose fitted half-light radii exceed the PSF half-width at half-maximum (HWHM), ensuring the objects are sufficiently resolved for reliable Sérsic measurements. After applying this resolution cut, we retained 17 protocluster and 32 field LAEs in F150W, and 16 protocluster and 23 field LAEs in F277W with reliable size measurements. We verified our size measurements using independent fitting with Galight (Ding et al. 2020) and PetroFit (Geda et al. 2022), confirming consistent size estimates across methodologies (detailed morphological analysis in Laishram et al., in preparation). Effective radii were converted from angular to physical units (kpc) using the angular diameter distance at  $z = 4.90$ . Uncertainties on all median values reported in this work are estimated using non-parametric bootstrap resampling: for each sample, we draw  $N$  values with replacement from the observed data (where  $N$  is the sample size) and compute the median, repeating this procedure 10,000 times. The reported uncertainties correspond to the 16th and 84th percentiles of the bootstrap distribution (68% confidence interval), yielding asymmetric error bars. For comparisons between two samples (e.g.,  $\Delta$ median), we perform joint bootstrapping, independently resampling both samples in each iteration and computing the difference of medians, with uncertainties again derived from the 68% confidence interval of the resulting distribution. Statistical significance is assessed using both Mann-Whitney  $U$  tests and Kolmogorov-Smirnov tests (two-sided), which are non-parametric and do not assume Gaussian distributions.

## 4. RESULTS

### 4.1. Morphological Properties

We compare the structural properties of protocluster and field LAEs using Sérsic profile fits in both rest-frame UV (F150W) and rest-frame optical (F277W)

imaging (Figures 2 and 3). The effective radii reveal a wavelength-dependent environmental signal.

At rest-optical wavelengths, protocluster LAEs exhibit larger effective radii with median  $R_e = 0.81^{+0.26}_{-0.04}$  kpc, compared to  $R_e = 0.58^{+0.11}_{-0.04}$  kpc for field LAEs, corresponding to a  $\simeq 40\%$  increase in median size. A Mann-Whitney  $U$  test yields  $p = 0.041$  ( $2.0\sigma$ ), suggesting a difference at marginal significance. LAEs associated with the three secondary overdensity peaks show rest-optical sizes comparable to or slightly above the field median, but the differences are not statistically significant for any individual peak (Mann-Whitney  $p = 0.40$ – $0.91$ ), in contrast to the significant enhancement observed for the primary protocluster members.

In rest-UV, this size difference is absent. Protocluster LAEs have median effective radius  $R_e = 0.68^{+0.08}_{-0.10}$  kpc, compared to  $R_e = 0.53^{+0.20}_{-0.06}$  kpc for field LAEs. A Mann-Whitney  $U$  test yields  $p = 0.51$  ( $0.7\sigma$ ), indicating no statistically significant difference in rest-UV sizes between protocluster and field environments. This wavelength-dependent result indicates that protocluster LAEs possess more extended stellar distributions at rest-optical wavelengths, where older stellar populations contribute, while no significant environmental difference is detected in rest-UV sizes tracing recent star formation.

In contrast to the effective radii, Sérsic indices show no statistically significant environmental dependence in either band. In rest-optical, protocluster and field LAEs have comparable median values of  $n = 0.57^{+0.15}_{-0.25}$  and  $n = 0.65^{+0.08}_{-0.20}$ , respectively (Mann-Whitney  $p = 0.70$ ); in rest-UV, the corresponding values are  $n = 0.52^{+0.79}_{-0.22}$  and  $n = 0.43^{+0.24}_{-0.02}$  ( $p = 0.40$ ). This indicates that the central concentration of LAE light profiles is not measurably affected by the protocluster environment at this epoch. We do not detect significant environmental differences in Ly $\alpha$  equivalent width ( $p = 0.42$ ), UV luminosity ( $p = 0.24$ ), or specific star formation rate ( $p = 0.48$ ). In contrast, the rest-frame optical sizes show the clearest environmental separation in our current dataset. We confirmed that using F115W (rest-NUV  $\sim 1950\text{\AA}$ ) instead of F150W yields a consistent result: protocluster LAEs show slightly larger median sizes but the difference is not statistically significant ( $p = 0.12$ ).

### 4.2. Size-Mass Relation and Residual Analysis

To account for the well-established correlation between galaxy size and stellar mass, we examined the size-mass relations separately for each environment (Figure 2). For the field sample, we fit a linear relation of the form  $\log_{10}(R_e/\text{kpc}) = \alpha + \beta \log_{10}(M_*/M_\odot)$  to the

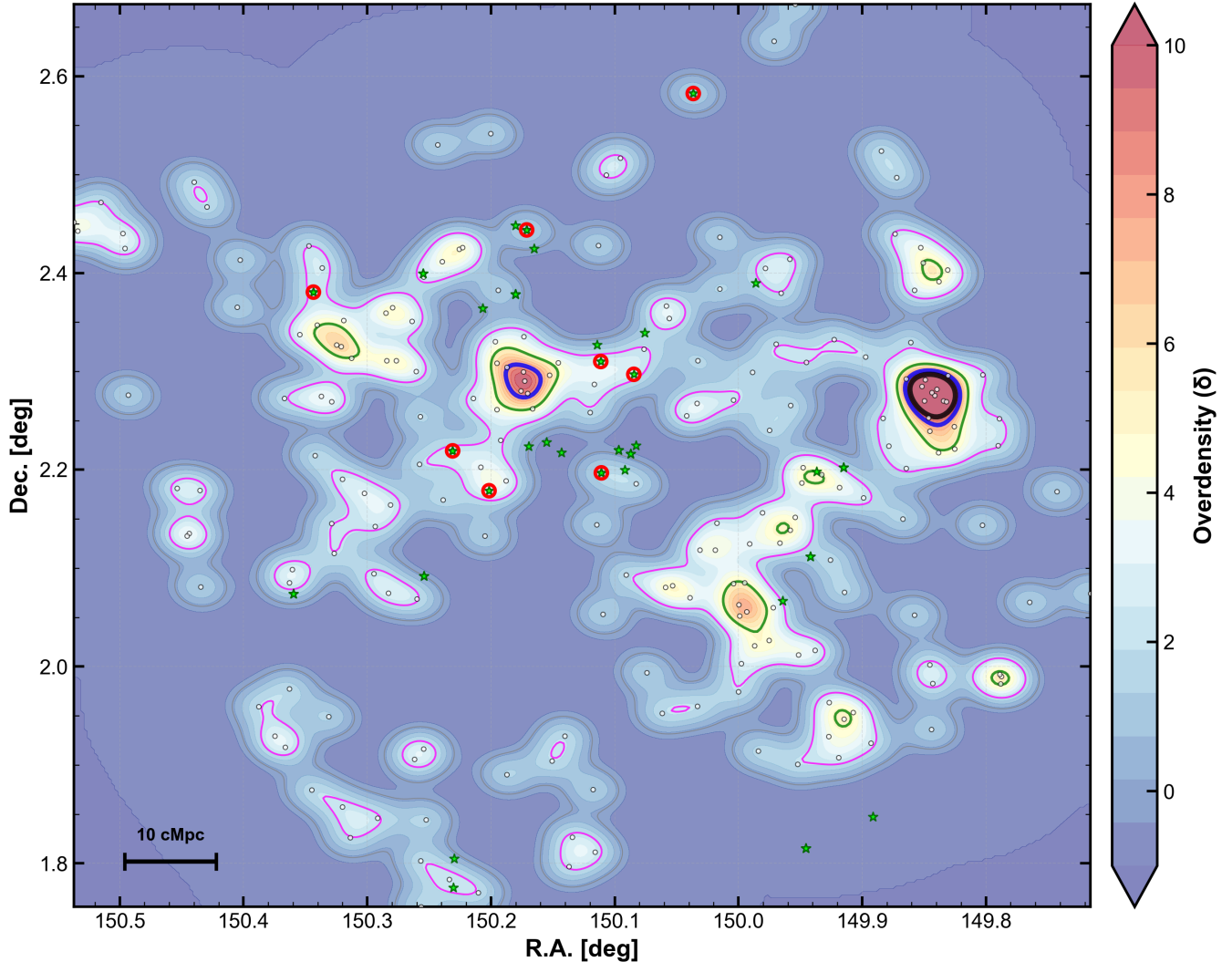


**Figure 1.** Overdensity map of NB718 LAEs at  $z = 4.90$  revealing a large-scale protocluster structure (the Loktak protocluster) within the  $0.54 \text{ deg}^2$  COSMOS-Web survey area. The color-coded background represents the smoothed density field derived from Gaussian kernel density estimation (KDE), with warmer colors indicating higher overdensity as shown by the colorbar ( $\delta$ ). Contour lines trace overdensity levels at  $\delta = 2$  (magenta),  $\delta = 5$  (green),  $\delta = 8$  (blue), and  $\delta = 10$  (black). Individual LAE positions are shown as white open circles. Spectroscopically confirmed galaxies at  $z \simeq 4.9$  are marked as green stars, while those cross-matched with our LAE sample (within  $0.5''$ ) are further highlighted with red open circles overlaid on the stars. The structure exhibits a prominent primary peak (4-fold surface density enhancement within  $1.5 \text{ pMpc}$  radius), along with three additional significant peaks at distances of  $7.6$ ,  $6.0$ , and  $11.1 \text{ pMpc}$  from the center, forming an interconnected protocluster complex spanning  $\sim 65 \times 36 \text{ cMpc}^2$  characteristic of large-scale structure at this epoch.

F277W measurements using ordinary least squares. The field relation yields a slope  $\beta = 0.12 \pm 0.06$  and intercept  $\alpha = -1.2 \pm 0.5$  with a scatter of  $0.15 \text{ dex}$ . To visualize the size-mass trend and reduce scatter from individual measurements, we computed binned median sizes in stellar mass bins. The sample was divided into equal-width mass bins, and for each bin containing sufficient galaxies, we calculated the median size and its uncertainty via bootstrap resampling (10,000 iterations). These binned medians are displayed in Figure 2 as large filled symbols (circles for field, squares for protocluster LAEs) with

error bars representing bootstrap uncertainties and horizontal bars indicating bin widths.

Figure 2 reveals that protocluster LAEs systematically lie above the field size-mass relation at rest-frame optical wavelengths. For comparison, Figure 2 also shows the rest-optical size-mass relations from Song et al. (2026) for LAEs at  $z \simeq 4-7$  and from Allen et al. (2025) for SFGs at  $z \simeq 4-6$ . Our field LAEs are broadly consistent with the Song et al. (2026) LAE relation, while our protocluster LAEs are shifted above it, indicating rest-optical sizes enhanced beyond the typical

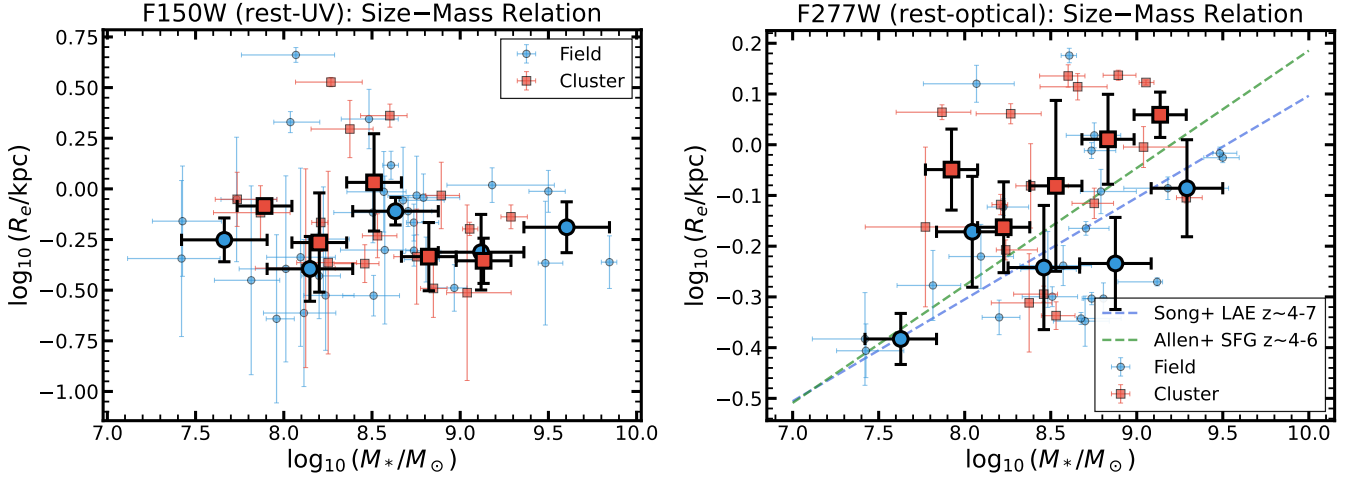


**Figure 2.** Size-mass relations for LAEs in rest-UV (F150W, left panel) and rest-optical (F277W, right panel). Blue circles represent field LAEs, and red squares represent protocluster members. Large filled symbols show binned medians with bootstrap uncertainties. In the left panel (rest-UV), no systematic offset is detected between protocluster and field LAEs (field fit:  $\beta = 0.05 \pm 0.08$ , scatter = 0.2 dex), although the large intrinsic scatter limits the sensitivity to environmental differences. In the right panel (rest-optical), protocluster LAEs systematically lie above the field relation, indicating larger sizes at fixed stellar mass. The median rest-optical size enhancement is  $\simeq 40\%$  (cluster median  $R_e = 0.81$  kpc vs. field 0.58 kpc). For reference, the right panel includes the rest-optical size-mass relations from Song et al. (2026) for LAEs at  $z \simeq 4-7$  (blue dashed line) and from Allen et al. (2025) for star-forming galaxies (SFGs) at  $z \simeq 4-6$  (green dashed line). Field LAEs are broadly consistent with the Song et al. (2026) LAE relation (Section 4.2).

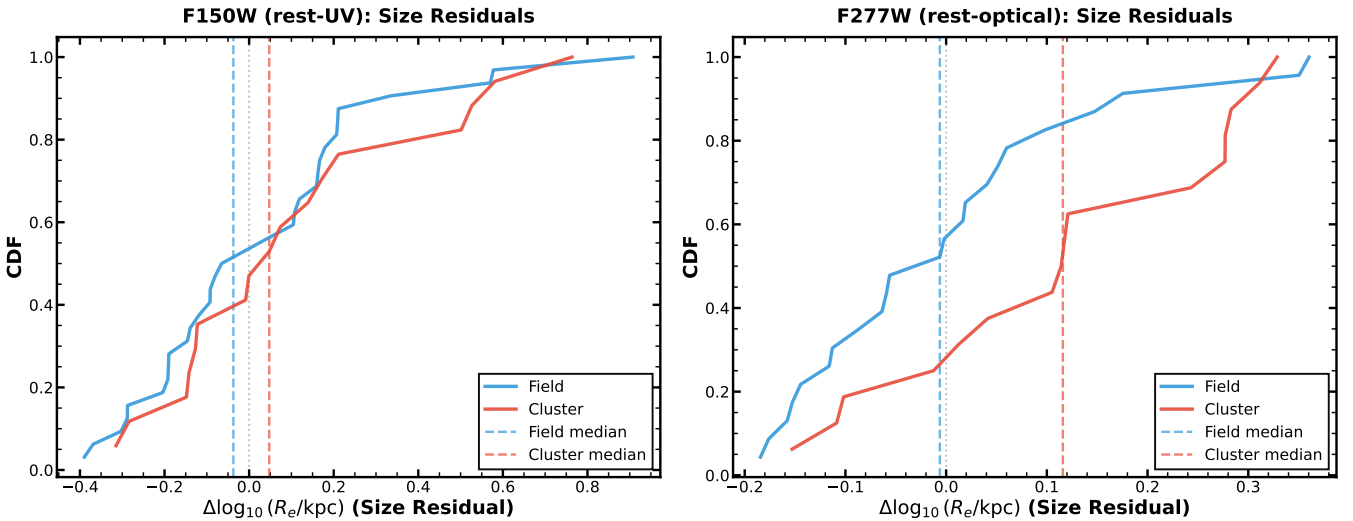


**Figure 3.** Cumulative distribution functions (CDFs) of size residuals  $\Delta \log_{10}(R_e)$  from the field size-mass relation for rest-frame UV (F150W, left) and rest-frame optical (F277W, right). Residuals are calculated as the observed size minus the size predicted from the linear relation fit to our field LAE sample (Section 4.2) at each galaxy’s stellar mass. Blue lines show field LAEs (centered near zero by construction), and red lines show protocluster LAEs. In rest-UV (left panel), the distributions are statistically indistinguishable (KS  $p = 0.79$ ; Mann-Whitney  $p = 0.42$ ). In rest-optical (right panel), protocluster LAEs show positive residuals (median  $\Delta \log_{10}(R_e) = +0.12^{+0.07}_{-0.04}$  dex; Mann-Whitney  $p = 0.033$ ,  $2.1\sigma$ ; KS  $p = 0.029$ ), indicating they are  $\simeq 31\%$  larger than field galaxies of comparable stellar mass.

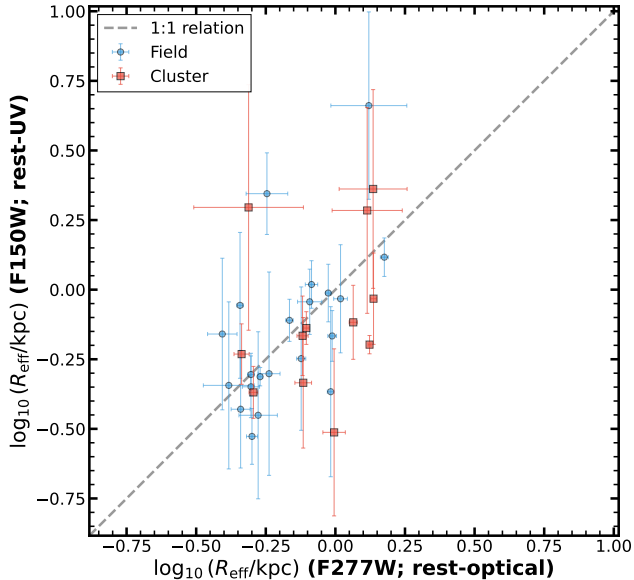


**Figure 4.** Comparison of rest-UV (F150W) and rest-optical (F277W) effective radii for protocluster (red squares) and field (blue circles) LAEs with valid size measurements in both bands. The dashed line indicates the 1:1 relation; galaxies below the line have more compact UV emission relative to their optical extent ( $R_{e,UV} < R_{e,opt}$ ). Field LAEs are broadly consistent with the 1:1 relation within their scatter. Protocluster LAEs tend to lie below the 1:1 line, but this difference is not statistically significant. The trend is consistent with the significant rest-optical size enhancement identified in the independent single-band comparisons (Figures 2–3), which shifts protocluster LAEs to larger optical sizes while no corresponding difference is detected in rest-UV.

LAE size-mass scaling. In rest-frame UV (F150W), the field relation has  $\beta = 0.05 \pm 0.08$  and  $\alpha = -0.6 \pm 0.7$  with a scatter of 0.2 dex. In F150W, no systematic offset is detected between protocluster and field LAEs, although the larger intrinsic scatter in rest-UV (0.2 dex, consistent with Allen et al. 2025) limits the sensitivity to environmental differences at these wavelengths.

To quantify deviations from the expected size-mass scaling, we computed size residuals for each galaxy as  $\Delta \log_{10}(R_e) = \log_{10}(R_{e,obs}) - \log_{10}(R_{e,pred})$ , where  $R_{e,pred}$  is the size predicted from the linear relation fit to our field LAE sample in each respective filter (Section 4.2) at the galaxy’s stellar mass. Figure 3 presents the cumulative distribution functions (CDFs) of size residuals for both samples. In F277W, protocluster LAEs exhibit predominantly positive residuals (median  $\Delta \log_{10}(R_e) = +0.12^{+0.07}_{-0.04}$  dex), indicating they are systematically  $\approx 31\%$  larger than field galaxies of comparable stellar mass. The field sample is centered near zero by construction (median  $\Delta \log_{10}(R_e) = -0.01^{+0.02}_{-0.05}$  dex). The difference between the two median residuals is

+0.12 dex (68% CI: [+0.08, +0.21]). Both a Mann-Whitney  $U$  test ( $p = 0.033$ ,  $2.1\sigma$ ) and a Kolmogorov-Smirnov test ( $p = 0.029$ ) indicate that the residual distributions differ, with 75% of protocluster LAEs showing positive residuals compared to 44% of field LAEs.

In F150W, the residual distributions for protocluster and field samples are statistically indistinguishable (Mann-Whitney  $p = 0.42$ ,  $0.8\sigma$ ), with protocluster median residual +0.05 dex and field median  $-0.04$  dex. This is consistent with no size difference at rest-UV wavelengths after accounting for stellar mass. The wavelength-dependent behavior indicates that the environmental size enhancement is driven by processes affecting extended stellar populations traced by rest-optical light, rather than the rest-UV sizes tracing recent star formation, where no significant environmental difference is detected. A direct comparison for galaxies with reliable sizes in both bands (13 protocluster and 21 field LAEs passing PSF cuts in both F150W and F277W; Figure 4) is consistent with this result: protocluster LAEs tend to lie below the 1:1 relation, but the difference in UV-to-optical size ratio between environments is not statistically significant.

## 5. DISCUSSION

### 5.1. Comparison with LAE Size Measurements at $z \approx 5$

Our field LAE sample at  $z = 4.90$  shows median rest-optical (F277W) effective radius  $R_e = 0.58^{+0.11}_{-0.04}$  kpc, consistent with the characteristically compact sizes ( $R_e \lesssim 1$  kpc) of LAEs observed across a wide range of redshifts (Kim et al. 2026). Stacking analysis of LAEs at  $z \approx 5.7$  in the COSMOS field revealed disk-like light profiles (Sérsic  $n \sim 0.7$ ; Taniguchi et al. 2009), consistent with the low Sérsic indices found in our sample. This is also in agreement with the size-mass relation measured by Song et al. (2026) for 876 spectroscopically confirmed LAEs at  $4 < z < 7$ , who found that LAE sizes closely match those of typical SFGs in both slope and normalization at these redshifts, with statistically comparable UV and optical sizes ( $\log(R_{e,V}/R_{e,UV}) \approx 0.03$ ).

In contrast, our protocluster LAEs exhibit a larger median  $R_e = 0.81^{+0.26}_{-0.04}$  kpc, a  $\sim 40\%$  increase over the field. This size enhancement occurs without a corresponding change in Sérsic index ( $p = 0.70$ ), indicating that protocluster LAEs maintain similar light profile shapes to field LAEs while possessing more extended stellar distributions in the rest-optical.

### 5.2. Environmental Effects on Galaxy Morphology in Protoclusters

While environmental effects on galaxy morphology have been studied in several protoclusters at  $z \lesssim 3$ , no previous work has examined the morphological properties of LAEs in rest-frame optical in protocluster environments at  $z \gtrsim 4$ . At lower redshifts, rest-optical HST WFC3 F160W observations of 151 H $\alpha$  emitters (HAEs) in protoclusters at  $z \simeq 2.23$  found similar Sérsic index distributions between protocluster and field populations (Golden-Marx et al. 2025), consistent with the absence of environmental trends in rest-UV morphology for UV-selected star-forming galaxies at similar redshifts (Peter et al. 2007). The morphology-density relation was found to be already in place at  $z \simeq 2$  in CARLA clusters at  $1.4 < z < 2.8$  (Mei et al. 2023). At  $z \simeq 1.5$ , [O II] emitters in an extreme overdensity showed a higher frequency of morphological disturbances and relatively larger sizes in the densest regions compared to the field, along with elevated star formation activity (Laishram et al. 2024). At  $z = 4.3$ , ALMA dust continuum observations of dusty star-forming galaxies (DSFGs) in the SPT2349–56 protocluster core found no significant difference in half-light radii compared to field DSFGs (Hill et al. 2020). Image stacking of proto-brightest cluster galaxy (proto-BCG) candidates at  $z \simeq 4$  revealed  $\sim 28\%$  larger rest-UV effective radii compared to magnitude-matched field galaxies (Ito et al. 2019), although this enhancement applies to the most luminous UV-selected protocluster members, a population distinct from the lower-mass LAEs studied here. Overzier et al. (2008) studied LAEs in the TN J1338–1942 protocluster at  $z = 4.1$  using *HST* ACS rest-UV imaging and found no evidence for environmental differences in sizes or morphologies, although the broad photometric redshift selection ( $\Delta z \sim 0.5$ ) may dilute any environmental signal. This rest-UV null result is consistent with our finding of no significant size difference at rest-UV wavelengths ( $p = 0.51$ ), suggesting that the environmental signature we detect is accessible only at rest-frame optical wavelengths. Our study extends these efforts to  $z = 4.90$  with the addition of JWST rest-frame optical imaging, revealing that the environmental size enhancement in protocluster LAEs emerges specifically in the extended stellar populations traced by longer wavelengths — a signal that was inaccessible to previous rest-UV-only studies.

Environmental dependence of galaxy sizes has been established at lower redshifts: a study of  $> 3$  million galaxies (stellar mass  $\log M_*/M_\odot \gtrsim 8.9$ – $9.9$ , with the lower completeness limit increasing with redshift) from Hyper Suprime-Cam at  $0.3 < z < 0.7$  found galaxies in denser environments are  $\sim 10$ – $20\%$  larger in rest-optical than counterparts matched in stellar mass and morphology in lower-density regions (Ghosh et al. 2024). How-

ever, these studies focused on massive, mass-selected galaxy populations at  $z \lesssim 1$ . Our observed  $\sim 40\%$  rest-optical size enhancement at  $z = 4.90$  ( $\sim 31\%$  at fixed stellar mass from residual analysis) represents the first such measurement for LAEs in a protocluster environment. Direct comparison with the low-redshift results is limited by differences in galaxy populations (LAEs vs. mass-selected samples) and selection methods, but the detection of an environmental size signal at this early epoch suggests that processes influencing galaxy structure are already operating in protocluster environments during the first  $\sim 1.2$  Gyr of cosmic history.

### 5.3. Size-Mass Relations in Different Environments

Recent JWST studies have established the rest-optical size-mass relation for high-redshift galaxies, with slopes consistent across different populations and redshifts (Song et al. 2026; Allen et al. 2025). Our field LAE relation is consistent with these results within the uncertainties (Section 4.2). The key environmental result is in the normalization: at fixed stellar mass, protocluster LAEs are systematically offset toward larger rest-optical sizes.

At lower redshifts, some studies of star-forming galaxies in protocluster environments have found no significant environmental effect on the size-mass relation: H $\alpha$  emitters (HAEs) in protoclusters at  $z \simeq 2$  show similar rest-frame UV sizes to field HAEs at fixed stellar mass (Naufal et al. 2023), and mass-matched star-forming samples at  $z < 0.5$  show no rest-optical size difference between cluster and field environments (Chen et al. 2024). Our results at  $z = 4.90$  show that even among star-forming LAEs, the protocluster environment produces a measurable offset in rest-optical sizes at fixed stellar mass (Figure 2), with a median residual of  $\Delta \log_{10}(R_e) = +0.12$  dex (68% CI:  $[+0.08, +0.21]$ ). This suggests that environmental size enhancement may already be in place for star-forming populations at this epoch, preceding the quiescent-dominated effects seen at  $z < 2$ .

### 5.4. Wavelength-Dependent Size Measurements

Multi-wavelength size measurements have revealed that galaxies can exhibit different effective radii when observed at different rest-frame wavelengths. Allen et al. (2025) measured rest-optical and rest-UV size-mass relations for star-forming galaxies at  $z = 3$ – $9$  and found that the rest-UV size-mass relation has both a steeper slope and larger intrinsic scatter ( $\sigma \sim 0.22$ – $0.25$  dex) compared to rest-optical ( $\sigma \sim 0.17$ – $0.19$  dex), with low-mass galaxies at  $z > 5$  being  $> 2\sigma$  smaller in rest-UV than in rest-optical. In contrast, Ono et al. (2024) found

the average  $r_{e,\text{opt}}/r_{e,\text{UV}} \approx 1.01$  across  $z = 4\text{--}10$ , suggesting that on average UV and optical sizes remain comparable at these epochs. Our result shows a wavelength-dependent environmental signature: protocluster LAEs are significantly larger in rest-optical but not in rest-UV compared to field LAEs. This contrasts with the general LAE population at  $z \gtrsim 4.9$ , where rest-UV and rest-optical sizes are statistically comparable (Song et al. 2026), suggesting that the protocluster environment introduces a wavelength-dependent structural difference not present in the general field population.

The physical basis for wavelength-dependent sizes reflects differences in stellar populations: rest-UV light traces young, massive stars formed over the last  $\sim 100$  Myr, while rest-optical light is more sensitive to older stellar populations (Papovich et al. 2005). Studies of stellar population gradients have shown these are the dominant factor ( $\sim 80\%$ ) driving wavelength-dependent effective radii, with differential dust attenuation contributing secondarily (Baes et al. 2024). In this context, the wavelength-dependent environmental signature we observe (Section 4.1) suggests that protocluster processes preferentially affect the extended older stellar populations rather than the central regions where current star formation is concentrated. In the protocluster environment, where the galaxy surface density is enhanced by a factor of  $\sim 4$  relative to the field, several processes could contribute to this wavelength-dependent signature. Tidal interactions among neighboring galaxies can redistribute existing stellar material to larger radii, while accretion of smaller companions (e.g., Shimizu & Umemura 2010) may deposit stars preferentially in the galaxy outskirts, building up an extended rest-optical envelope around the compact star-forming core. Additionally, an earlier onset of star formation in the overdense environment could allow more time to accumulate spatially extended older stellar populations traced by rest-optical light. With the present data, we cannot distinguish among these scenarios, and multiple processes may operate simultaneously. Disentangling their relative contributions will require larger LAE samples across multiple protoclusters, complemented by deeper photometric and spectroscopic data at these redshifts. The absence of a significant environmental difference in rest-UV sizes is consistent with the characteristically compact UV morphologies of LAEs observed across  $z \simeq 2\text{--}6$  (Paulino-Afonso et al. 2018; Shibuya et al. 2019; Song et al. 2026). Indeed, compact rest-UV morphology is closely linked to Ly $\alpha$  photon escape, as LAEs with higher equivalent widths tend to be smaller and more concentrated (Paulino-Afonso et al. 2018); this implies that this rest-UV null

result may partly reflect a selection effect, since LAEs are by definition drawn from the compact end of the UV size distribution. Moreover, Ly $\alpha$  photons in evolved LAEs can escape through low-density channels in the ISM cleared by outflows (Shimizu et al. 2025); in the protocluster environment, tidal interactions may similarly disrupt the ISM, potentially facilitating Ly $\alpha$  escape while also producing the larger rest-optical sizes we observe.

Future wide-field spectroscopic surveys (e.g., Subaru/PFS) combined with JWST imaging of additional protoclusters at similar redshifts will be needed to determine whether this wavelength-dependent size enhancement is a general feature of LAEs in overdense environments. Spatially resolved spectroscopy (e.g., JWST/NIRSpec IFU) would further enable measurements of stellar population gradients and gas kinematics to constrain the physical processes driving the observed size differences.

## 6. CONCLUSIONS

We have investigated the morphological properties of Ly $\alpha$  emitters in the Loktak protocluster, a large-scale structure at  $z = 4.90$  in the COSMOS field, using JWST NIRCcam imaging from COSMOS-Web. From a sample of 177 clean LAEs identified in the NB718 SILVERRUSH catalog, we define 28 protocluster members (within 3.0 pMpc of the primary overdensity center) and 44 field LAEs (bottom 25% overdensity). Our main findings are:

(1) We identify a large-scale overdensity structure spanning  $\sim 65 \times 36$  cMpc<sup>2</sup>, comprising four distinct peaks with surface density enhancements of up to  $\sim 4$  times relative to the overall surveyed region within 1.5 pMpc radii. The primary peak encloses 18 LAEs within 1.5 pMpc and exhibits a 4-fold surface density enhancement.

(2) We measure rest-frame UV (F150W,  $\sim 2540\text{\AA}$ ) and rest-frame optical (F277W,  $\sim 4700\text{\AA}$ ) morphologies via Sérsic profile fitting. After applying PSF resolution cuts, we retain 17 (32) protocluster (field) LAEs in F150W and 16 (23) in F277W.

(3) Protocluster LAEs exhibit larger effective radii than field LAEs in rest-frame optical wavelengths (median  $R_e = 0.81^{+0.26}_{-0.04}$  kpc vs.  $0.58^{+0.11}_{-0.04}$  kpc; Mann-Whitney  $p = 0.041$ ,  $2.0\sigma$ ), corresponding to a  $\sim 40\%$  size increase. This environmental signal is absent in rest-frame UV, where protocluster and field sizes are statistically indistinguishable ( $p = 0.51$ ).

(4) The size-mass residual analysis supports this result: at fixed stellar mass, protocluster LAEs in F277W are offset by  $\Delta \log_{10}(R_e) = +0.12$  dex (68% CI:

[+0.08, +0.21]; Mann-Whitney  $p = 0.033$ ,  $2.1\sigma$ ; KS  $p = 0.029$ ) above the field relation. Sérsic indices show no significant environmental dependence ( $p = 0.70$  in F277W).

(5) This wavelength-dependent size enhancement suggests that protocluster environments at  $z \simeq 5$  preferentially influence extended stellar populations traced by rest-optical light, with no significant environmental difference detected in the rest-UV sizes tracing recent star formation.

As one of the first rest-frame optical morphological studies of LAEs in a protocluster environment at this redshift, our results provide initial evidence for wavelength-dependent environmental effects but are based on a single structure with modest sample sizes. Extending these measurements to additional protoclus-

ters across  $4 < z < 6$ , with larger samples and deeper imaging, will be essential to determine whether this environmental signature is a universal feature of LAE evolution in overdense regions or specific to this system.

- 1 This work was supported by JSPS KAKENHI grant No.
- 2 J23H01219 and JSPS Core-to-Core Program (grant No.:
- 3 JPJSCCA20210003). H.K. acknowledges support from
- 4 JSPS KAKENHI grant Nos. 23KJ2148 and 25K17444.
- 5 SK acknowledges support from JSPS KAKENHI grant
- 6 Nos. 24KJ0058 and 24K17101. TK acknowledges fi-
- 7 nancial support from JSPS KAKENHI Grant Numbers
- 8 24H00002 (Specially Promoted Research by T. Kodama
- 9 et al.), 22K21349 (International Leading Research by
- 10 S. Miyazaki et al.), and JSPS Core-to-Core Program
- 11 (JPJSCCA20210003; M. Yoshida et al.).

## REFERENCES

- Aihara, H., AlSayyad, Y., Ando, M., et al. 2019, PASJ, 71, 114, doi: [10.1093/pasj/psz103](https://doi.org/10.1093/pasj/psz103)
- . 2022, PASJ, 74, 247, doi: [10.1093/pasj/psab122](https://doi.org/10.1093/pasj/psab122)
- Allen, N., Oesch, P. A., Toft, S., et al. 2025, A&A, 698, A30, doi: [10.1051/0004-6361/202452690](https://doi.org/10.1051/0004-6361/202452690)
- Arnouts, S., Moscardini, L., Vanzella, E., et al. 2002, MNRAS, 329, 355, doi: [10.1046/j.1365-8711.2002.04988.x](https://doi.org/10.1046/j.1365-8711.2002.04988.x)
- Ata, M., Lee, K.-G., Vecchia, C. D., et al. 2022, Nature Astronomy, 6, 857, doi: [10.1038/s41550-022-01693-0](https://doi.org/10.1038/s41550-022-01693-0)
- Baes, M., Mosenkov, A., Kelly, R., et al. 2024, A&A, 683, A182, doi: [10.1051/0004-6361/202348419](https://doi.org/10.1051/0004-6361/202348419)
- Bond, N. A., Gawiser, E., Guaita, L., et al. 2012, ApJ, 753, 95, doi: [10.1088/0004-637X/753/2/95](https://doi.org/10.1088/0004-637X/753/2/95)
- Boquien, M., Burgarella, D., Roehlly, Y., et al. 2019, A&A, 622, A103, doi: [10.1051/0004-6361/201834156](https://doi.org/10.1051/0004-6361/201834156)
- Boselli, A., & Gavazzi, G. 2006, PASP, 118, 517, doi: [10.1086/500691](https://doi.org/10.1086/500691)
- Bruzual, G., & Charlot, S. 2003, MNRAS, 344, 1000, doi: [10.1046/j.1365-8711.2003.06897.x](https://doi.org/10.1046/j.1365-8711.2003.06897.x)
- Bădescu, T., Yang, Y., Bertoldi, F., et al. 2017, ApJ, 845, 172, doi: [10.3847/1538-4357/aa8220](https://doi.org/10.3847/1538-4357/aa8220)
- Calzetti, D., Armus, L., Bohlin, R. C., et al. 2000, ApJ, 533, 682, doi: [10.1086/308692](https://doi.org/10.1086/308692)
- Capak, P. L., Riechers, D., Scoville, N. Z., et al. 2011, Nature, 470, 233, doi: [10.1038/nature09681](https://doi.org/10.1038/nature09681)
- Casey, C. M., Kartaltepe, J. S., Drakos, N. E., et al. 2023, ApJ, 954, 31, doi: [10.3847/1538-4357/acc2bc](https://doi.org/10.3847/1538-4357/acc2bc)
- Chen, Z., Gu, Y., Zou, H., & Yuan, Q. 2024, ApJ, 961, 253, doi: [10.3847/1538-4357/ad15fd](https://doi.org/10.3847/1538-4357/ad15fd)
- Chiang, Y.-K., Overzier, R. A., Gebhardt, K., & Henriques, B. 2017, ApJL, 844, L23, doi: [10.3847/2041-8213/aa7e7b](https://doi.org/10.3847/2041-8213/aa7e7b)
- Cooper, M. C., Newman, J. A., Madgwick, D. S., et al. 2005, ApJ, 634, 833, doi: [10.1086/432868](https://doi.org/10.1086/432868)
- Darvish, B., Mobasher, B., Sobral, D., Scoville, N., & Aragon-Calvo, M. 2015, ApJ, 805, 121, doi: [10.1088/0004-637X/805/2/121](https://doi.org/10.1088/0004-637X/805/2/121)
- Ding, X., Silverman, J., Treu, T., et al. 2020, ApJ, 888, 37, doi: [10.3847/1538-4357/ab5b90](https://doi.org/10.3847/1538-4357/ab5b90)
- Dressler, A. 1980, ApJ, 236, 351, doi: [10.1086/157753](https://doi.org/10.1086/157753)
- Franco, M., Akins, H. B., Casey, C. M., et al. 2024, ApJ, 973, 23, doi: [10.3847/1538-4357/ad5e6a](https://doi.org/10.3847/1538-4357/ad5e6a)
- Franco, M., Casey, C. M., Koekemoer, A. M., et al. 2025, arXiv e-prints, arXiv:2506.03256, doi: [10.48550/arXiv.2506.03256](https://doi.org/10.48550/arXiv.2506.03256)
- Geda, R., Crawford, S. M., Hunt, L., et al. 2022, AJ, 163, 202, doi: [10.3847/1538-3881/ac5908](https://doi.org/10.3847/1538-3881/ac5908)
- Ghosh, A., Urry, C. M., Powell, M. C., et al. 2024, ApJ, 971, 142, doi: [10.3847/1538-4357/ad596f](https://doi.org/10.3847/1538-4357/ad596f)
- Golden-Marx, E., Cai, Z., Shi, D., et al. 2025, arXiv e-prints, arXiv:2511.14843, doi: [10.48550/arXiv.2511.14843](https://doi.org/10.48550/arXiv.2511.14843)
- Harish, S., Kartaltepe, J. S., Liu, D., et al. 2025, ApJ, 992, 45, doi: [10.3847/1538-4357/adfa1e](https://doi.org/10.3847/1538-4357/adfa1e)
- Higuchi, R., Ouchi, M., Ono, Y., et al. 2019, ApJ, 879, 28, doi: [10.3847/1538-4357/ab2192](https://doi.org/10.3847/1538-4357/ab2192)
- Hill, R., Chapman, S., Scott, D., et al. 2020, MNRAS, 495, 3124, doi: [10.1093/mnras/staa1275](https://doi.org/10.1093/mnras/staa1275)
- Hu, W., Wang, J., Infante, L., et al. 2021, Nature Astronomy, 5, 485, doi: [10.1038/s41550-020-01291-y](https://doi.org/10.1038/s41550-020-01291-y)
- Huang, Y., Lee, K.-S., Cucciati, O., et al. 2022, ApJ, 941, 134, doi: [10.3847/1538-4357/ac9ea7](https://doi.org/10.3847/1538-4357/ac9ea7)

- Ilbert, O., Arnouts, S., McCracken, H. J., et al. 2006, *A&A*, 457, 841, doi: [10.1051/0004-6361:20065138](https://doi.org/10.1051/0004-6361:20065138)
- Inoue, A. K., Yamanaka, S., Ouchi, M., et al. 2020, *PASJ*, 72, 101, doi: [10.1093/pasj/psaa100](https://doi.org/10.1093/pasj/psaa100)
- Ito, K., Kashikawa, N., Toshikawa, J., et al. 2019, *ApJ*, 878, 68, doi: [10.3847/1538-4357/ab1f0c](https://doi.org/10.3847/1538-4357/ab1f0c)
- Khostovan, A. A., Kartaltepe, J. S., Salvato, M., et al. 2026, *ApJS*, 282, 6, doi: [10.3847/1538-4365/ae1cb9](https://doi.org/10.3847/1538-4365/ae1cb9)
- Kikuta, S., Ouchi, M., Shibuya, T., et al. 2023, *ApJS*, 268, 24, doi: [10.3847/1538-4365/ace4cb](https://doi.org/10.3847/1538-4365/ace4cb)
- Kim, K. J., Alavi, A., Snapp-Kolas, C., et al. 2026, *ApJ*, 996, 117, doi: [10.3847/1538-4357/ae1d6c](https://doi.org/10.3847/1538-4357/ae1d6c)
- Kusakabe, H., Shimasaku, K., Ouchi, M., et al. 2018, *PASJ*, 70, 4, doi: [10.1093/pasj/psx148](https://doi.org/10.1093/pasj/psx148)
- Laishram, R., Kodama, T., Morishita, T., et al. 2024, *ApJL*, 964, L33, doi: [10.3847/2041-8213/ad3238](https://doi.org/10.3847/2041-8213/ad3238)
- Lee, K.-S., Dey, A., Hong, S., et al. 2014a, *ApJ*, 796, 126, doi: [10.1088/0004-637X/796/2/126](https://doi.org/10.1088/0004-637X/796/2/126)
- . 2014b, *ApJ*, 796, 126, doi: [10.1088/0004-637X/796/2/126](https://doi.org/10.1088/0004-637X/796/2/126)
- Lee, K.-S., Gawiser, E., Park, C., et al. 2024, *ApJ*, 962, 36, doi: [10.3847/1538-4357/ad165e](https://doi.org/10.3847/1538-4357/ad165e)
- Malavasi, N., Lee, K.-S., Dey, A., et al. 2021, *ApJ*, 921, 103, doi: [10.3847/1538-4357/ac1c6e](https://doi.org/10.3847/1538-4357/ac1c6e)
- Mei, S., Hatch, N. A., Amodeo, S., et al. 2023, *A&A*, 670, A58, doi: [10.1051/0004-6361/202243551](https://doi.org/10.1051/0004-6361/202243551)
- Morishita, T., Liu, Z., Stiavelli, M., et al. 2025, *ApJ*, 982, 153, doi: [10.3847/1538-4357/adb30f](https://doi.org/10.3847/1538-4357/adb30f)
- Naufal, A., Koyama, Y., Shimakawa, R., & Kodama, T. 2023, *ApJ*, 958, 170, doi: [10.3847/1538-4357/acfb81](https://doi.org/10.3847/1538-4357/acfb81)
- Ono, Y., Harikane, Y., Ouchi, M., et al. 2024, *PASJ*, 76, 219, doi: [10.1093/pasj/psae004](https://doi.org/10.1093/pasj/psae004)
- Ouchi, M., Ono, Y., & Shibuya, T. 2020, *ARA&A*, 58, 617, doi: [10.1146/annurev-astro-032620-021859](https://doi.org/10.1146/annurev-astro-032620-021859)
- Ouchi, M., Harikane, Y., Shibuya, T., et al. 2018, *PASJ*, 70, S13, doi: [10.1093/pasj/psx074](https://doi.org/10.1093/pasj/psx074)
- Overzier, R. A. 2016, *A&A Rv*, 24, 14, doi: [10.1007/s00159-016-0100-3](https://doi.org/10.1007/s00159-016-0100-3)
- Overzier, R. A., Bouwens, R. J., Cross, N. J. G., et al. 2008, *ApJ*, 673, 143, doi: [10.1086/524342](https://doi.org/10.1086/524342)
- Papovich, C., Dickinson, M., Giavalisco, M., Conselice, C. J., & Ferguson, H. C. 2005, *ApJ*, 631, 101, doi: [10.1086/429120](https://doi.org/10.1086/429120)
- Paulino-Afonso, A., Sobral, D., Ribeiro, B., et al. 2018, *MNRAS*, 476, 5479, doi: [10.1093/mnras/sty281](https://doi.org/10.1093/mnras/sty281)
- Peng, C. Y., Ho, L. C., Impey, C. D., & Rix, H.-W. 2002, *AJ*, 124, 266, doi: [10.1086/340952](https://doi.org/10.1086/340952)
- Peter, A. H. G., Shapley, A. E., Law, D. R., et al. 2007, *ApJ*, 668, 23, doi: [10.1086/521184](https://doi.org/10.1086/521184)
- Ramakrishnan, V., Moon, B., Im, S. H., et al. 2023, *ApJ*, 951, 119, doi: [10.3847/1538-4357/acd341](https://doi.org/10.3847/1538-4357/acd341)
- Ramakrishnan, V., Lee, K.-S., Artale, M. C., et al. 2024, *ApJ*, 977, 119, doi: [10.3847/1538-4357/ad83cb](https://doi.org/10.3847/1538-4357/ad83cb)
- Ramella, M., Boschini, W., Fadda, D., & Nonino, M. 2001, *A&A*, 368, 776, doi: [10.1051/0004-6361:20010071](https://doi.org/10.1051/0004-6361:20010071)
- Rubet, M., Menéndez-Delmestre, K., Gonçalves, T. S., et al. 2025, *ApJ*, 991, 35, doi: [10.3847/1538-4357/adf18c](https://doi.org/10.3847/1538-4357/adf18c)
- Shibuya, T., Ouchi, M., Harikane, Y., & Nakajima, K. 2019, *ApJ*, 871, 164, doi: [10.3847/1538-4357/aaf64b](https://doi.org/10.3847/1538-4357/aaf64b)
- Shibuya, T., Ouchi, M., Konno, A., et al. 2018, *PASJ*, 70, S14, doi: [10.1093/pasj/psx122](https://doi.org/10.1093/pasj/psx122)
- Shimasaku, K., Ouchi, M., Okamura, S., et al. 2003, *ApJL*, 586, L111, doi: [10.1086/374880](https://doi.org/10.1086/374880)
- Shimizu, I., & Umemura, M. 2010, *MNRAS*, 406, 913, doi: [10.1111/j.1365-2966.2010.16758.x](https://doi.org/10.1111/j.1365-2966.2010.16758.x)
- Shimizu, S., Kashikawa, N., Kikuta, S., et al. 2025, *MNRAS*, 542, 3125, doi: [10.1093/mnras/staf1377](https://doi.org/10.1093/mnras/staf1377)
- Shuntov, M., Akins, H. B., Paquereau, L., et al. 2025, *A&A*, 704, A339, doi: [10.1051/0004-6361/202555799](https://doi.org/10.1051/0004-6361/202555799)
- Song, Q., Liu, F. S., Ren, J., et al. 2026, *ApJ*, 997, 126, doi: [10.3847/1538-4357/ae24e4](https://doi.org/10.3847/1538-4357/ae24e4)
- Staab, P., Lemaux, B. C., Forrest, B., et al. 2024, *MNRAS*, 528, 6934, doi: [10.1093/mnras/stae301](https://doi.org/10.1093/mnras/stae301)
- Taniguchi, Y., Murayama, T., Scoville, N. Z., et al. 2009, *ApJ*, 701, 915, doi: [10.1088/0004-637X/701/2/915](https://doi.org/10.1088/0004-637X/701/2/915)